EDGE ARTICLE

Cooperative reversible assembly in triply interlocked Al$_6$L$_4$ and Ga$_6$L$_4$ cages

Ignacio Izquierdo, [ID] [a] Laura Martínez-Castro, [ID] [b] Gregori Ujaque [ID] [b] and Antonio J. Martínez-Martínez [ID] *[a]

Understanding and controlling the assembly of mechanically interlocked molecules remains a significant challenge. Formation of mechanically interlocked metal–organic cages has, to date, relied exclusively on transition metals due to their predictable coordination geometries and robust bonding. Here, we report, for the first time, the reversible assembly of mechanically interlocked cages based on main-group metals, Al$_6$L$_4$ and Ga$_6$L$_4$. Structural and computational analyses reveal helical [2]catenane quadruple-decker cage topologies stabilized by six metal–ligand nodes, bridging μ-OH groups, extensive π-stacking, and directional CH···O interactions. Remarkably, simple acid–base cycling triggers fully reversible cage unlocking–recatenation processes in water at room temperature. Unlike transition-metal-mediated cage interlocking, they assemble instantaneously and selectively *via* an unprecedented cooperative main-group interlocking pathway, without detectable monomeric cage intermediates. Thermodynamic analyses reveal metal-dependent switching, involving entropy-driven disassembly coupled to strongly enthalpy-driven reassembly, with the Ga$_6$L$_4$ cage ∼500-fold more stable than Al$_6$L$_4$. These findings provide fundamental understanding of new assembly dynamics beyond conventional transition metals.

Introduction

Mechanically interlocked molecules, including catenanes,[1–7] rotaxanes,[8–13] clippanes[14] and molecular knots,[15–23] enable unique controlled molecular motion, gated transport and stimuli-responsive behaviour.[24,25] Because their mechanical bonds can only be disrupted by covalent cleavage, these topologically complex architectures underpin emerging technologies from molecular machines,[26,27] stimulus-gated catalysis[28,29] to adaptive materials and soft robotics.[30–34] However, precisely controlling their assembly remains a fundamental challenge. Covalent synthetic routes offer exact connectivity but lack error correction, whereas purely non-covalent methods typically compromise directional precision.[35] In contrast, metal-directed self-assembly is a powerful tool, combining predictable coordination geometries, thermodynamic error correction, and tunable lability of metal–ligand bonds.[36,37] These features enable the formation of mechanically interlocked metal–organic architectures (Fig. 1) whose cavity size, shape, and charge can be encoded during self-assembly.

Since Fujita's seminal report of the first mechanically interlocked metal–organic cage, a triply interwoven [2]catenane M$_6$L$_4$ structure assembled using Pd or Pt,[38] the field has expanded rapidly. Numerous examples have been developed exclusively using transition metals, including Co,[39] Cu,[40] Zn,[39,41] Ru,[42,43] Rh,[44–46] Pd,[47–56] Ag[57] and Pt.[58,59] These cage assemblies exhibit diverse stimulus-responsive functionalities, such as shape-switching,[48,50,54,56] high-affinity guest binding,[51] and artificial-muscle-like actuation.[44] However, reversible mechanical interlocking switching under mild conditions, essential for programmable and responsive supramolecular function, remains rare.[60,61] Main-group metals offer an orthogonal and unexplored toolkit for switchable mechanical interlocking. Although some examples of discrete monomeric main-group metal–organic cages have been developed,[62–74] mechanical interlocking involving such metals remains completely unexplored.
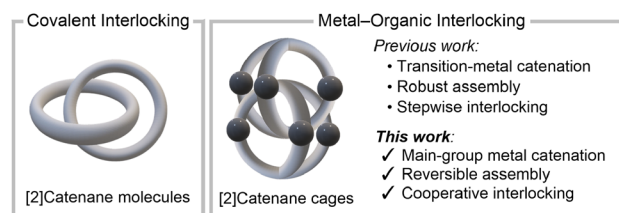
[a]Department of Chemistry and Center for Research in Sustainable Chemistry (CIQSO), Supramolecular Organometallic and Main Group Chemistry Laboratory, University of Huelva, Huelva 21007, Spain. E-mail: antonio.martinez@dqcm.uhu.es

[b]Departamento de Química, Centro de Innovación en Química Avanzada (ORFEO-CINQA), Universitat Autònoma de Barcelona, 08193 Cerdanyola, Spain

Fig. 1 From covalent to metal–organic interlocking: transition-metal *vs.* main-group metal-mediated catenation (this work).

Here we introduce first examples of mechanically interlocked metal–organic cages assembled from main-group metals, Al_6L_4 **IC1** and Ga_6L_4 **IC2**. Through a simple tritopic ligand, H_6L, we demonstrate fully reversible acid–base-triggered disassembly and reassembly of their triply interwoven helical [2] catenane topologies in water at room temperature. In contrast to transition-metal cage interlocking assembly, which typically proceeds through dimerization of monomeric cage intermediates, they assemble instantaneously *via* an unprecedented cooperative main-group pathway, without detectable monomeric M_3L_2 cage intermediates. Thermodynamic analyses reveal a distinctive metal-dependent switching dynamics, driven by entropy during disassembly and enthalpy during reassembly, with the Ga_6L_4 cage exhibiting ~500-fold higher stability than its Al_6L_4 analogue.

Results and discussion

The tritopic ligand H_6L was obtained in two steps (Scheme 1a). A Cu-catalyzed three-fold alkyne–azide "click" reaction (CuAAC)[75,76] between 1,3,5-triethynylbenzene and 1-azido-2,3-dimethoxybenzene afforded the tris(1,2,3-triazole) precursor Me_6L (76%). Subsequent demethylation with BBr_3 gave H_6L quantitatively (95%). The terminal catechol groups offer robust chelation for oxophilic M^{3+} ions, while the rigid C_{3v} phenylene C_6H_3 core pre-arranges three metal binding sites within a trigonal array. Furthermore, the bridging triazole units add conformational adaptability and promote $\pi \cdots \pi/CH \cdots \pi$ stackings. Self-assembly of H_6L with $Al(acac)_3$ or $Ga(acac)_3$ (acac = acetylacetonate), and KOH in a ratio 4 : 6 : 9 in MeOH, selectively produced the triply interlocked cages Al_6L_4 **IC1** and Ga_6L_4 **IC2** within 16 hours at room temperature (Scheme 1b). This click-demethylation-assembly sequence provided **IC1** and **IC2** in 86% and 80% yield, respectively, after simple trituration with diethyl ether. Notably, **IC1**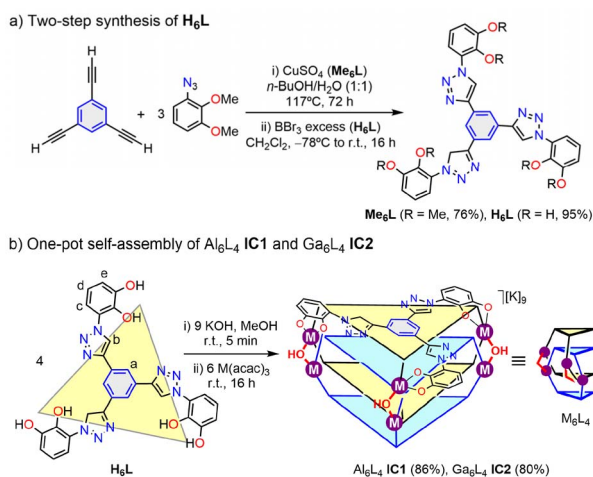 and **IC2** represent the first examples of mechanically interlocked metal–organic cages constructed exclusively from main-group metals.[60]

Disappearance of the catechol OH signals of H_6L (δ 10.05 and 9.52 ppm) in the ^1H NMR spectra of **IC1** and **IC2** confirms metal–catecholate coordination (Fig. 2a–d). Each interlocked cage displays two sets of sharp resonances in D_2O at 298 K, reflecting two chemically inequivalent ligand environments. This spectral duplication evidences the mechanical interpenetration of two cage monomeric units, Al_3L_2 **C1** or Ga_3L_2 **C2**, within each dimeric assembly. The triazole protons $H^b/H^{b'}$ shift downfield (**IC1**: δ 9.28/9.42 ppm; **IC2**: δ 9.26/9.36 ppm) relative to H_6L (δ 9.08 ppm), consistent with a peripheral cage location. In contrast, the phenylene C_6H_3 core protons $H^a/H^{a'}$ are strongly shielded (**IC1**: δ 7.70/7.36 ppm; **IC2**: δ 7.71/7.38 ppm; *vs.* H_6L: δ 8.52) owing to the π-stacking within the cage interior. ^{13}C NMR data in D_2O also shows duplicated sets at 298 K, confirming ligand interpenetration (Fig. S18 and S35, SI).

Complementary ^1H NMR in CD_3OD shows that the duplicated ligand resonances visible in D_2O coalesce into single broadened sets at 298 K. $H^b/H^{b'}$ appear as averaged and broad singlets at δ 9.12 (**IC1**) and 9.14 (**IC2**) ppm, and $H^a/H^{a'}$ at δ 8.43 (**IC1**) and 8.34 (**IC2**) ppm (Fig. S16 and S33, SI). This solvent-dependent modulation reflects the weaker hydrophobic/solvophobic driving force in CD_3OD relative to D_2O, which attenuates π-stacking in **IC1** and **IC2**, thereby reducing inner/outer chemical-shift differences ($\Delta\delta$) and averaging them on the NMR timescale at 298 K. Variable-temperature ^1H NMR in CD_3OD (318–238 K) progressively resolves these resonances as exchange slows upon cooling to 238 K. At 238 K, the ligand resonances desymmetrize, $H^b/H^{b'}$ resolve into five (**IC1**) and four (**IC2**) partially overlapping broad singlets spanning δ 9.04–9.31 ppm and δ 9.31–9.60 ppm, respectively. Likewise, $H^a/H^{a'}$ split into five (**IC1**) and three (**IC2**) overlapping broad singlets δ 8.38–8.80 ppm and δ 8.29–8.37 ppm, respectively; with the catecholate $H^c/H^d/H^e$ showing analogous behavior (Fig. S55 and S56, SI). Warming up to 298 K restores the initial state. These low-temperature spectra are consistent with freezing of the interlocked topologies **IC1** and **IC2**, where four ligands are arranged in a non-equivalent fashion (*vide infra*).

High-resolution ESI-TOF MS (negative mode) confirmed the M_6L_4 formulation for **IC1** and **IC2**. Each spectrum displays isotopically resolved series of peaks for intact anions $[Al_6L_4]^{n-}$ (for **IC1**) and $[Ga_6L_4]^{n-}$ (for **IC2**) in charge states 4−, 3−, and 2−, detected as Na^+/K^+ adducts drawn from the ionization medium (Fig. 2e and f). A second family of peaks reveals that each cage retains three hydroxide OH^- groups. **IC1** gives representative peaks at m/z 940.0542 (3−) and 1438.0436 (2−) for $[Al_6L_4(OH)_3 + xA]^{n-}$, whereas **IC2** furnishes an analogous series at m/z 763.4597 (4−), 1030.9328 (3−) and 1549.9055 (2−) for $[Ga_6L_4(OH)_3 + xA]^{n-}$ (A = Na^+, K^+). In addition, in-source collisional activation cleaves each interlocked assembly into units $[Al_3L_2]^{3-}$ **C1** (m/z 425.0564) and $[Ga_3L_2]^{3-}$ **C2** (m/z 467.6689), evidencing mechanical unlocking of **IC1** and **IC2** during ionization.

Single crystals of Me_6L suitable for X-ray diffraction were obtained by slow evaporation of a concentrated EtOAc solution (50 mM, 0.5 mL) at room temperature over 24 h. The crystal

Scheme 1 (a) Synthesis of ligands Me_6L and H_6L. (b) Self-assembly of triply interlocked quadruple-decker cages Al_6L_4 **IC1** and Ga_6L_4 **IC2**. Isolated yields are shown in parenthesis.
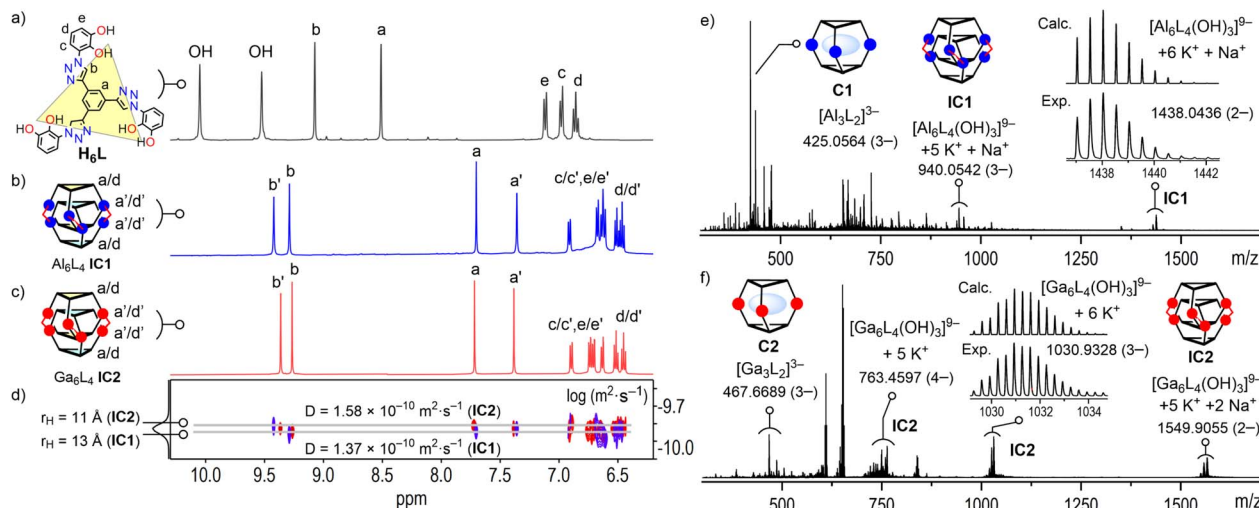
Fig. 2 (a) ^{1}H NMR spectra (400 MHz, 298 K) of ligand H_6L in DMSO-d_6, (b) cage Al_6L_4 IC1 (blue) and (c) Ga_6L_4 IC2 (red) in D_2O; duplicated ligand environments are labelled with a/d and a'/d'. (d) Overlay of DOSY NMR (400 MHz, 298 K) for IC1 and IC2 in D_2O. (e) ESI-TOF HR mass spectra (negative mode) of IC1 and (f) IC2, showing selected peaks for interlocked cages $[M_6L_4]^{n-}$ and $[M_3L_2]^{n-}$ C1 and C2 units.

structure of Me_6L reveals a planar 1,3,5-phenylene C_6H_3 core flanked by three peripheral 1,2,3-triazoles, promoting extended ligand conjugation (Fig. 3a). The catechol termini are pre-organized at distances of ~15.1 Å, ideal for chelating remote M^{3+} nodes. Packing is governed by $\pi\cdots\pi$ contacts (centroid⋯centroid 3.7483(9) Å) supplemented by C–H⋯π/Me⋯π/C–H⋯N interactions (Fig. 3b and c), underscoring the intrinsic propensity of this ligand framework for stacking. DOSY NMR studies corroborate a significant aggregation of both Me_6L and H_6L in solution. The measured diffusion coefficients (D) of 3.10 × 10^{-10} m^2 s^{-1} for Me_6L and 2.60 × 10^{-10} m^2 s^{-1} for H_6L correspond to Stokes–Einstein hydrodynamic radii (r_H) of 9 and 11 Å (Fig. S57 and S58, SI), respectively, roughly twice the esti-mated monomer size (6 Å) and consistent with predominant dimer aggregation. This pre-organization is expected to reduce the entropic cost of cage assembly using H_6L.
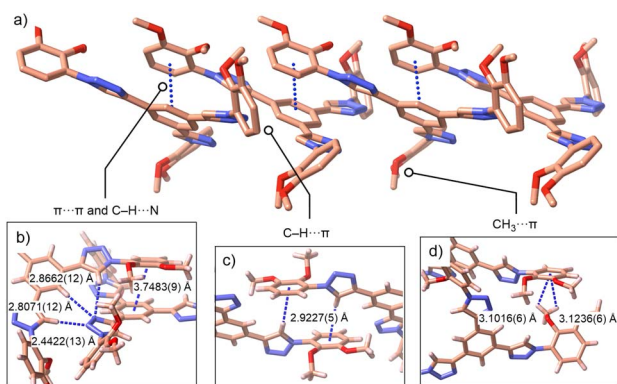
Single crystals of the cage Ga_6L_4 IC2 suitable for X-ray diffraction, as its potassium salt form $K_9[Ga_6L_4(OH)_3]$, were grown by vapor diffusion of acetone (2 mL) into a 1 : 1 H_2O/MeOH solution of the cage (10 mM, 0.5 mL) at room tempera-ture over one week. These crystals confirm the anticipated triply interlocked [2]catenane topology (Fig. 4). Two mechanically threaded monomeric units Ga_3L_2 C2 (cage I and cage II) are connected by six Ga–catecholate chelate nodes (Ga–O 1.8926(18)–1.9544(19) Å). At each of the three crossing nodes a μ-OH bridge spans a Ga_2 unit (Ga–OH 1.890(2)–1.928(2) Å), rendering every Ga^{3+} center five-coordinate within the anionic $[Ga_6L_4(OH)_3]^{9-}$ framework. Each Ga_3L_2 C2 cage encloses a prolate cavity with 6.8180(18) and 6.7422(19) Å inter-deck spacings and voids of 83 and 107 Å^3 (calculated using CageCa-vityCalc-C3),[77] ideally sized to host the tris(triazole)phenylene hub of its interpenetrating Ga_3L_2 partner (Fig. 4b). ESP mapping shows a uniformly negative potential inside each cavity, reflecting the π-rich ligand walls in each formal Ga_3L_2 C2 unit, suggesting that dispersion, π-stacking and Ga–O coordination likely drive interlocking.

Additional NCI analyses of DFT-optimized (B3LYP-D3/6-31g*) structures of IC1 and IC2 provided deeper insights into the non-covalent forces underpinning these assemblies. The presence of diffuse attractive isosurfaces highlights extensive π-stacking between ligand layers in both interlocked assemblies IC1 and IC2 (Fig. S97 and S98, SI). The distinct interaction maps, despite similar, suggest greater stability of the cage IC2 compared to IC1 through enhanced π-stacking (slightly larger and greener surfaces).

Four ligand decks form an eclipsed π-stack (inter-deck phenylene centroid⋯centroid: 3.3691(17), 3.3753(19) and 3.4493(18) Å). These decks are successively rotated by 17.28(3)–29.16(3)°, generating P/M helices that crystallize as a racemate in $P\bar{1}$ space group (P-helix is shown, Fig. 4c). An additional π-staircase array of contacts between triazoles (3.5120(19)–

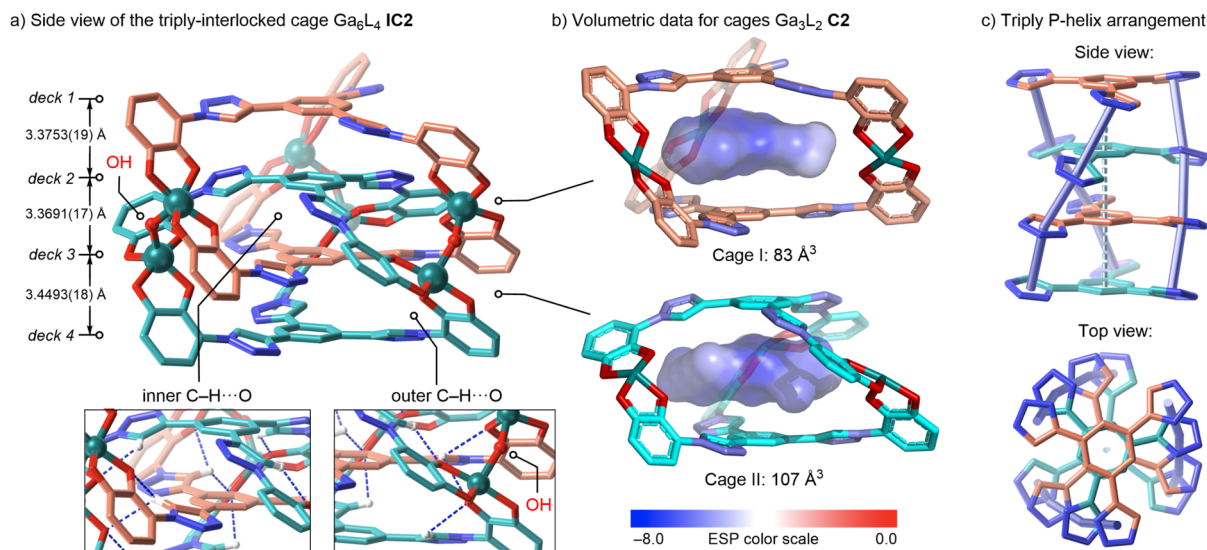

Fig. 3 Crystal packing of Me_6L highlighting key non-covalent inter-actions: (a) side-on view of a slipped stack showing π-overlap, (b) close-up of π⋯π and C–H⋯N contacts, (c) representative CH⋯π contacts and (d) Me⋯π interactions.

a) Side view of the triply-interlocked cage Ga₆L₄ **IC2**

b) Volumetric data for cages Ga₃L₂ **C2**

c) Triply P-helix arrangement

Fig. 4 Crystal structure of the triply interlocked cage Ga_6L_4 **IC2** (anionic form $[Ga_6L_4(OH)_3]^{9-}$). (a) Side view of the quadruple-decker assembly; μ-OH bridges and Ga atoms are shown ball–sticks, and key CH⋯O contacts as dashed lines. (b) Isolated Ga_3L_2 **C2** units (cage I and cage II) rendered with internal voids as ESP isosurfaces calculated using CageCavityCalc-C3 (grid size 0.7 Å, eem charge model). (c) P-Helical arrangement of the four ligand decks (side and top). H atoms (except those in CH⋯O contacts), K^+ ions, and solvent are omitted; C beige/cyan, N blue, O red, Ga teal.

4.044(2) Å), supported by directional internal CH⋯O interactions (2.266(2)–2.782(2) Å), further consolidate this quadruple-decker. When interlocked, three tris(triazole)-phenylene cores remain planar (Fig. 4a: decks 1, 3 and 4), whereas one bends (deck 2) to accommodate the interlocked array **IC2**, underscoring the adaptive flexibility of the ligand L^{6-} framework. In addition, these discrete anionic interlocked $[Ga_6L_4(OH)_3]^{9-}$ cages pack into a three-dimensional lattice via outer-sphere K^+ bridges and solvent channels (Fig. S95, SI).

The four ligands are crystallographically non-equivalent in **IC2**, partitioning into two inner and two outer decks. This solid-state asymmetry rationalizes the inner/outer twofold NMR splitting observed D_2O solution and the further desymmetrisation observed in CD_3OD at 238 K. Moreover, $^1H,^1H$-NOESY cross-peaks between inner phenylene $H^{a'}$ and outer triazole H^b confirm face-edge proximity required for the quadruple-decker helix (Fig. S22 and S39, SI). Additional inter-deck $H^a/H^{a'}$ NOESY contacts between neighboring phenylene C_6H_3 cores confirm retention of the π-stacking motif of **IC1** and **IC2** in solution. DOSY experiments further supports intact cage architectures in D_2O solution (**IC1**: $D = 1.37 \times 10^{-10}$ m² s⁻¹; **IC2**: $D = 1.58 \times 10^{-10}$ m² s⁻¹, both in D_2O, Fig. 2d), yielding r_H of 13 and 11 Å, respectively, demonstrating retention of the interlocked topologies in water (estimated crystallographic radii of 13 Å for **IC2**, see SI). Additional DOSY results in CD_3OD solution (**IC1**: $D = 2.75 \times 10^{-10}$ m² s⁻¹, $r_H = 13$ Å; **IC2**: $D = 2.90 \times 10^{-10}$ m² s⁻¹, $r_H = 12$ Å) closely matching the structural cage dimensions, confirming intact interlocked topologies in both D_2O and CD_3OD.

Motivated by the unique topological features and the presence of stabilizing μ-OH bridges, we examined the response of the cages **IC1** and **IC2** to protonation. Titration of solutions of **IC1** and **IC2** with incremental additions of deutero-hydrochloric acid (DCl) in D_2O were monitored by ^1H NMR (Fig. 5). Cage **IC1** underwent rapid structural disruption upon addition of one equivalent of acid as evidenced by progressive disappearance and broadening of the cage resonances after four equivalents (Fig. S64, SI). By contrast, cage **IC2** remains intact until the third equivalent of acid, underscoring its higher kinetic and thermodynamic robustness (Fig. 5a). Remarkably, subsequent neutralization with sodium deuteroxide (NaOD, 1–4 equiv.) fully restores the diagnostic spectra of each interlocked cage **IC1** and **IC2**. While **IC1** recatenates after 3–4 equivalents of base, **IC2** readily interlocks after one equivalent. Identical spectral changes were obtained across the window 1–5 mM, the highest range permitted by the solubility of **IC1** and **IC2**, demonstrating a fully reversible unlocking/recatenation process. The absence of resonances attributable to monomeric M_3L_2 cages **C1** or **C2** further supports a highly cooperative and effectively direct assembly pathway under these conditions.

Lyophilization of the acidified solutions allowed us to analyze the unlocked intermediates resulting from disassembling both cages, **IC1** and **IC2**. ESI-TOF mass analysis reveal dominant ions at m/z 626.1121 (2−) and 669.0500 (2−) corresponding to partially protonated species $[Al_2(H_xL)_2]^{n-}$ and $[Ga_2(H_xL)_2]^{n-}$ (Fig. S74 and S85, SI). The absence of higher-mass ions suggests that protonation lowers the net charge, favoring H-bonded "$M_2(H_xL)_2$" species that exchange rapidly in D_2O solution and thus broaden the ^1H NMR signals during disassembly. Notably, under these partially acidified conditions (4 equiv.), the dominant $[M_2(H_xL)_2]^{n-}$ ions do not contain OH⁻ groups, in contrast to the intact cage $[M_6L_4(OH)_3]^{n-}$ ions, where μ-OH bridging is implicit. This indicates protonation/disruption of the μ-OH bridges during unlocking; conversely,
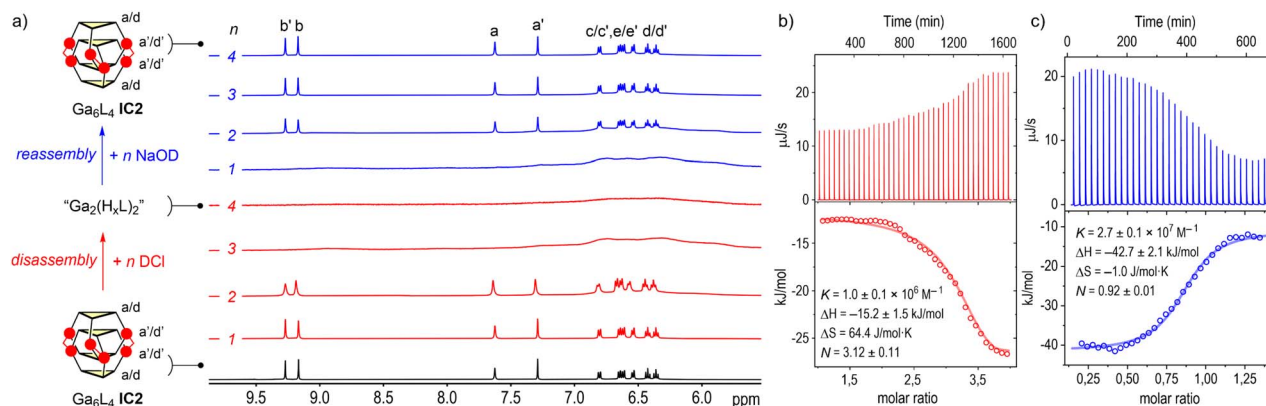
Fig. 5 Reversible acid–base switching of the interlocked cage Ga_6L_4 **IC2**: (a) ^1H NMR (500 MHz, 298 K, 4 mM) stack for Ga_6L_4 **IC2** during titration with DCl (1–4 equiv., red) and back-titration with NaOD (1–4 equiv., blue) in D_2O (identical spectra are obtained in the 1–5 mM range). ITC traces: (b) disassembly (1–4 equiv. of DCl) and (c) reassembly (0–1.5 equiv. of NaOD) of **IC2** in D_2O (1 mM) at 298 K.

reappearance of the **IC1** and **IC2** resonances upon neutralization with base correlates with re-formation of these bridges. IR spectroscopy showed a broad $\nu(OH)$ at 3500 cm^{-1} and ^1H NMR in DMSO-d_6 confirming partial catechol reprotonation (Fig. S81–S84, SI). Together, these observations indicate that full deprotonation of H_6L and intact μ-OH bridges are pre-requisites for cage assembly.

While controlled addition of acid (1–4 equiv.) resulted in partial protonated "$M_2(H_xL)_2$" species, addition of a large excess of acid (30 equiv.) fully protonated the system, regenerating back the neutral ligand H_6L. To map the direct interlocking pathway, we conducted *in situ* NMR monitoring starting from the fully protonated ligand H_6L. Titration of H_6L with incremental additions of NaOD (1–6 equiv.) in D_2O generates the hexaanionic ligand species, L^{6-}, in its sodium form Na_6L (Fig. S68–S70, SI). DOSY NMR analysis reveals a significant dimeric pre-organization of Na_6L in solution ($D = 2.08 \times 10^{-10}$ $m^2 s^{-1}$, $r_H = 9$ Å), akin to Me_6L and H_6L. Addition of two equivalents of $AlCl_3$ and $GaCl_3$ as water soluble sources of Al^{3+} and Ga^{3+} ions, immediately produced the duplicated ligand ^1H NMR resonances of **IC1** and **IC2**. Although partial replacement of the bridging μ-OH groups for μ-Cl and outer-sphere exchange of K^+ for Na^+ cannot be excluded under these conditions, the formation of **IC1** and **IC2** is essentially instantaneous (<2 min), underscoring the high kinetic facility of this unusual main-group interlocking process. The rapid assembly is consistent with cooperative metal–catecholate chelation together with a hydrophobic/solvophobic contribution that further strengthens π-stacking and releases structured solvent molecules and counterions from the cavity regions during the assembly of **IC1** and **IC2**. This essentially direct main-group interlocking pathway, occurring without detectable formation of monomeric cage intermediates M_3L_2 **C1** or **C2**, contrasts markedly with the established monomer-to-dimer interlocking pathways typical for transition-metal-mediated cage assemblies.[41,48,50,52,54,55,78]

To quantify the thermodynamic driving forces underlying the reversible assembly of **IC1** and **IC2**, isothermal titration calorimetry (ITC) was carried out under the same acid–base NMR cycling regimes at 1 mM concentrations (Fig. 5b, c and S72, SI). The ITC isotherms captured single cooperative transition equilibria for both the disassembly and reassembly of **IC1** and **IC2**, therefore, data were fitted to one-set-of-sites models (independent-sites/Wiseman). Hence, the overall macroscopic equilibria returned N (acid/base titrant equivalents per cage at the transition) and apparent macroscopic equilibrium constants K (M^{-1}) for the overall disassembly (cage + $nH^+ \rightleftarrows$ disassembled state) and reassembly (disassembled state + $nOH^- \rightleftarrows$ cage) modelled steps at the specific transition N equivalents. Acid-induced disassembly is entropy-driven ($T\Delta S > 0$, Fig. 6) for both cages **IC1** ($T\Delta S = 32.9$ kJ mol^{-1}) and **IC2** ($T\Delta S = 19.1$ kJ mol^{-1}), consistent with the gain in translational/rotational and conformational freedom upon releasing ligands and metal ions. The modest exothermicity (**IC1**: $\Delta H = -16.0$ kJ mol^{-1}; **IC2**: $\Delta H = -15.2$ kJ mol^{-1}) is attributed to protonation of μ-OH bridges and catecholate groups. Overall, unlocking is easier for **IC1** ($\Delta G = -48.9$ kJ mol^{-1}) than for **IC2** ($\Delta G = -34.3$ kJ mol^{-1}), consistent with the higher intrinsic stability of the Ga_6L_4 cage **IC2**. Consistently, the ITC stoichiometries indicate $N = 1.06 \pm 0.03$ acid equivalent per cage for **IC1** and $N = 3.12 \pm 0.11$ for **IC2** during disassembly, matching the macroscopic equivalence points seen by ^1H NMR titrations. Reassembly on base addition is strongly enthalpy-driven (**IC1**: $\Delta H = -42.1$ kJ mol^{-1}; **IC2**: $\Delta H = -42.7$ kJ mol^{-1}). This reflects
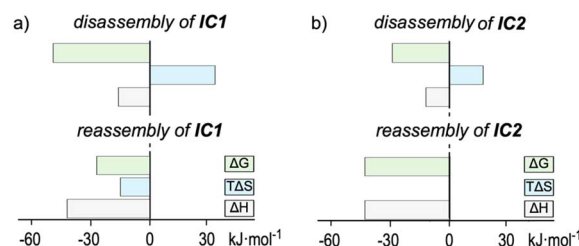

Fig. 6 Thermodynamic ITC data (ΔG, $T\Delta S$ and ΔH) for acid-induced disassembly and base-induced reassembly: (a) Al_6L_4 **IC1** and (b) Ga_6L_4 **IC2**.

the formation of twelve M–O chelate bonds and three μ-OH bridges, reinforced by dense $\pi \cdots \pi$ and C–H$\cdots$O contacts within the quadruple-decker stacks, providing a large exothermic gain that outweighs the desolvation costs. The reassembly entropy terms diverge. **IC1** pays a small entropic penalty ($T\Delta S = -15.3$ kJ mol^{-1}), whereas **IC2** incurs essentially none ($T\Delta S = -0.3$ kJ mol^{-1}). This reflects the balance between ordering penalties and the favorable hydrophobic/solvophobic release of structured solvent molecules and counterions from catecholate solvation shells and π-rich cavities during interlocking. We ascribe the minimal entropic term in **IC2** to a more extensive π-stacking and stronger Ga–O chelation, which together favor a more pre-organized unlocked ensemble and better compensates ordering in water compared to **IC1**. The resulting reassembly free energies (**IC1**: $\Delta G = -26.8$ kJ mol^{-1}; **IC2**: $\Delta G = -42.4$ kJ mol^{-1}) confirm the greater thermodynamic stability of the Ga$_6$L$_4$ cage **IC2**. In line with this, recatenation proceeds with $N = 3.62 \pm 0.04$ base equivalents per cage for **IC1** vs. $N = 0.92 \pm 0.01$ for **IC2**, again consistent with the ^{1}H NMR titrations. The obtained thermodynamic magnitudes are consistent with other metal–organic cages, where guest capture/assembly is generally exothermic and enthalpy-driven (typically $\Delta H \sim -20$ to -60 kJ mol^{-1}; $T\Delta S \sim -15$ to 25 kJ mol^{-1}), while release/exchange commonly shows favorable entropy ($T\Delta S > 10$ kJ mol^{-1}).[79–81]

At 298 K, the recatenation free energies are $\Delta G = -26.8$ kJ mol^{-1} ($K = 5.1 \times 10^4$ M^{-1}) for **IC1** and $\Delta G = -42.4$ kJ mol^{-1} ($K = 2.7 \times 10^7$ M^{-1}) for **IC2**. For unlocking, ΔG is -48.9 kJ mol^{-1} for **IC1** ($K = 3.7 \times 10^8$ M^{-1}) and -34.3 kJ mol^{-1} ($K = 1.0 \times 10^6$ M^{-1}) for **IC2**. The resulting $\Delta\Delta G$(**IC2–IC1**) $= -15.6$ kJ mol^{-1} for recatenation, corresponds to a $\sim$500-fold greater thermodynamic preference for the Ga$_6$L$_4$ cage **IC2** over the Al$_6$L$_4$ cage **IC1**. This metal dependence is consistent with the generally higher affinity of Ga–O chelation relative to Al–O (e.g., phenolate chelates exhibit $\log K \sim 31$ for Ga vs. 22 for Al in water),[82] reinforcing that stronger Ga–catecholate binding together with more extensive π-stacking, seen by NCI, stabilizes the triply interlocked Ga$_6$L$_4$ **IC2** topology.

Conclusions

We have demonstrated an unprecedented reversible assembly of the first examples of mechanically interlocked metal–organic cages involving main-group metals, Al$_6$L$_4$ and Ga$_6$L$_4$. A simple tritopic ligand, H$_6$L, directly folds each metal into helical, triply interwoven [2]catenane quadruple-decker topologies. Structural and computational studies confirm cage stabilization via six metal–ligand nodes, bridging μ-OH groups, extensive π-stacking and directional CH$\cdots$O interactions. Remarkably, simple acid–base cycling induces fully reversible cage disassembly–reassembly in water at room temperature. Unlike transition-metal-mediated cage interlocking, which typically assemble through detectable monomeric cages, this main-group metal assembly proceeds rapidly through an unusual cooperative pathway without observable monomeric M$_3$L$_2$ cage intermediates. Thermodynamic analyses reveal a metal-dependent switching behavior through entropy-driven unlocking coupled

with strongly enthalpy-driven recatenation. The Ga$_6$L$_4$ cage exhibits $\sim$500-fold higher stability than Al$_6$L$_4$ ($\Delta G = -42.4$ vs. -26.8 kJ mol^{-1}), reflecting enhanced Ga–ligand affinity and π-stacking. These results provide new fundamental insights into main-group metal-driven interlocking, thereby opening opportunities for novel stimuli-responsive supramolecular materials beyond conventional transition-metal systems.

Author contributions

I. I. conducted all experiments, synthesis, characterisation, NMR and ITC assembly studies. L. M. C. and G. U. performed electronic structure calculations of molecular models. A. J. M. M.: conceived the idea, project supervision, wrote the manuscript and conducted X-ray crystallography. All authors provided comments and approved the final version of the manuscript.

Conflicts of interest

There are no conflicts to declare.

Data availability

The datasets supporting this article have been uploaded as part of the Supplementary Information (SI). Supplementary information: experimental procedures, characterisation data, selected figures, crystallographic and computational details. See DOI: **https://doi.org/10.1039/d5sc05441a**.

CCDC 2467878 and 2467879 contain the supplementary crystallographic data for this paper.[83a,b]

Acknowledgements

References

1 Y. Wu, Q.-H. Guo, Y. Qiu, J. A. Weber, R. M. Young, L. Bancroft, Y. Jiao, H. Chen, B. Song, W. Liu, Y. Feng, X. Zhao, X. Li, L. Zhang, X.-Y. Chen, H. Li, M. R. Wasielewski and J. F. Stoddart, *Proc. Natl. Acad. Sci. U. S. A.*, 2022, **119**, e2118573119.

2 N. D. Colley, M. A. Nosiglia, S. L. Tran, G. H. Harlan, C. Chang, R. Li, A. O. Delawder, Y. Zhang and J. C. Barnes, *ACS Cent. Sci.*, 2022, **8**, 1672–1682.

3 A. Rodríguez-Rubio, A. Savoini, F. Modicom, P. Butler and S. M. Goldup, *J. Am. Chem. Soc.*, 2022, **144**, 11927–11932.

4 G. Gil-Ramírez, D. A. Leigh and A. J. Stephens, *Angew. Chem., Int. Ed.*, 2015, **54**, 6110–6150.

5 D. B. Amabilino, P. R. Ashton, V. Balzani, S. E. Boyd, A. Credi, J. Y. Lee, S. Menzer, J. F. Stoddart, M. Venturi and D. J. Williams, *J. Am. Chem. Soc.*, 1998, **120**, 4295–4307.

6 Y. Geerts, D. Muscat and K. Müllen, *Macromol. Chem. Phys.*, 1995, **196**, 3425–3435.

7 J.-L. Weidmann, J.-M. Kern, J.-P. Sauvage, D. Muscat, S. Mullins, W. Köhler, C. Rosenauer, H. J. Räder, K. Martin and Y. Geerts, *Chem.–Eur. J.*, 1999, **5**, 1841–1851.

8 J. Puigcerver, M. Marin-Luna, J. Iglesias-Sigüenza, M. Alajarin, A. Martinez-Cuevas and J. Berna, *J. Am. Chem. Soc.*, 2024, **146**, 2882–2887.

9 C.-F. Lee, D. A. Leigh, R. G. Pritchard, D. Schultz, S. J. Teat, G. A. Timco and R. E. P. Winpenny, *Nature*, 2009, **458**, 314–318.

10 M. Cirulli, A. Kaur, J. E. M. Lewis, Z. Zhang, J. A. Kitchen, S. M. Goldup and M. M. Roessler, *J. Am. Chem. Soc.*, 2019, **141**, 879–889.

11 M. C. Lipke, Y. Wu, I. Roy, Y. Wang, M. R. Wasielewski and J. F. Stoddart, *ACS Cent. Sci.*, 2018, **4**, 362–371.

12 C. J. Bruns and J. F. Stoddart, *Acc. Chem. Res.*, 2014, **47**, 2186–2199.

13 N. Solladié, J.-C. Chambron and J.-P. Sauvage, *J. Am. Chem. Soc.*, 1999, **121**, 3684–3692.

14 S. Ibáñez, C. Vicent and E. Peris, *Angew. Chem., Int. Ed.*, 2022, **61**, e202112513.

15 C. O. Dietrich-Buchecker, J. Guilhem, C. Pascard and J.-P. Sauvage, *Angew. Chem., Int. Ed. Engl.*, 1990, **29**, 1154–1156.

16 N. Ponnuswamy, F. B. L. Cougnon, J. M. Clough, G. D. Pantoş and J. K. M. Sanders, *Science*, 2012, **338**, 783–785.

17 Z. Ashbridge, E. Kreidt, L. Pirvu, F. Schaufelberger, J. H. Stenlid, F. Abild-Pedersen and D. A. Leigh, *Science*, 2022, **375**, 1035–1041.

18 D. A. Leigh, F. Schaufelberger, L. Pirvu, J. H. Stenlid, D. P. August and J. Segard, *Nature*, 2020, **584**, 562–568.

19 K. Caprice, D. Pál, C. Besnard, B. Galmés, A. Frontera and F. B. L. Cougnon, *J. Am. Chem. Soc.*, 2021, **143**, 11957–11962.

20 N. Ponnuswamy, F. B. L. Cougnon, G. D. Pantoş and J. K. M. Sanders, *J. Am. Chem. Soc.*, 2014, **136**, 8243–8251.

21 D. A. Leigh, J. J. Danon, S. D. P. Fielden, J.-F. Lemonnier, G. F. S. Whitehead and S. L. Woltering, *Nat. Chem.*, 2021, **13**, 117–122.

22 J. J. Danon, D. A. Leigh, S. Pisano, A. Valero and I. J. Vitorica-Yrezabal, *Angew. Chem., Int. Ed.*, 2018, **57**, 13833–13837.

23 J. E. Beves, J. J. Danon, D. A. Leigh, J.-F. Lemonnier and I. J. Vitorica-Yrezabal, *Angew. Chem., Int. Ed.*, 2015, **54**, 7555–7559.

24 A. W. Heard and S. M. Goldup, *ACS Cent. Sci.*, 2020, **6**, 117–128.

25 A. C. Pearcy and J. D. Crowley, *Chem.–Eur. J.*, 2023, **29**, e202203752.

26 V. Balzani, A. Credi, F. M. Raymo and J. F. Stoddart, *Angew. Chem., Int. Ed.*, 2000, **39**, 3348–3391.

27 I. Aprahamian, *ACS Cent. Sci.*, 2020, **6**, 347–358.

28 A. Martinez-Cuevas, A. Saura-Sanmartin, M. Alajarin and J. Berna, *ACS Catal.*, 2020, **10**, 7719–7733.

29 E. G. Percástegui, T. K. Ronson and J. R. Nitschke, *Chem. Rev.*, 2020, **120**, 13480–13544.

30 A. Saura-Sanmartin, A. Pastor, A. Martinez-Cuevas, G. Cutillas-Font, M. Alajarin and J. Berna, *Chem. Soc. Rev.*, 2022, **51**, 4949–4976.

31 J. E. M. Lewis, M. Galli and S. M. Goldup, *Chem. Commun.*, 2017, **53**, 298–312.

32 T. Ma, Y. Zhou, C. S. Diercks, J. Kwon, F. Gándara, H. Lyu, N. Hanikel, P. Pena-Sánchez, Y. Liu, N. J. Diercks, R. O. Ritchie, D. M. Proserpio, O. Terasaki and O. M. Yaghi, *Nat. Synth.*, 2023, **2**, 286–295.

33 J.-s. Geng, L. Mei, Y.-y. Liang, L.-y. Yuan, J.-p. Yu, K.-q. Hu, L.-h. Yuan, W. Feng, Z.-f. Chai and W.-q. Shi, *Nat. Commun.*, 2022, **13**, 2030.

34 H. V. Schröder, Y. Zhang and A. J. Link, *Nat. Chem.*, 2021, **13**, 850–857.

35 E. Du, X. Tang, W. Zhang, J. Dong, Y. Cui and Y. Liu, *Nat. Rev. Chem.*, 2025, **9**, 506–522.

36 M. Frank, M. D. Johnstone and G. H. Clever, *Chem.–Eur. J.*, 2016, **22**, 14104–14125.

37 Y. Yang, Y. Du, A. W. Heard and J. R. Nitschke, *Nat. Synth.*, 2025, **4**, 537–551.

38 M. Fujita, N. Fujita, K. Ogura and K. Yamaguchi, *Nature*, 1999, **400**, 52–55.

39 A. Westcott, J. Fisher, L. P. Harding, P. Rizkallah and M. J. Hardie, *J. Am. Chem. Soc.*, 2008, **130**, 2950–2951.

40 H.-M. Yu, M.-H. Du, J. Shu, Y.-H. Deng, Z.-M. Xu, Z.-W. Huang, Z. Zhang, B. Chen, P. Braunstein and J.-P. Lang, *J. Am. Chem. Soc.*, 2023, **145**, 25103–25108.

41 L. Yang, X. Jing, B. An, C. He, Y. Yang and C. Duan, *Chem. Sci.*, 2018, **9**, 1050–1057.

42 A. Mishra, A. Dubey, J. W. Min, H. Kim, P. J. Stang and K.-W. Chi, *Chem. Commun.*, 2014, **50**, 7542–7544.

43 S. Séjourné, A. Labrunie, C. Dalinot, D. Canevet, R. Guechaichia, J. Bou Zeid, A. Benchohra, T. Cauchy, A. Brosseau, M. Allain, C. Chamignon, J. Viger-Gravel, G. Pintacuda, V. Carré, F. Aubriet, N. Vanthuyne, M. Sallé and S. Goeb, *Angew. Chem., Int. Ed.*, 2024, **63**, e202400961.

44 L.-L. Dang, J. Zheng, J.-Z. Zhang, T. Chen, Y.-H. Chai, H.-R. Fu, F. Aznarez, S.-R. Liu, D.-S. Li and L.-F. Ma, *Angew. Chem., Int. Ed.*, 2024, **63**, e202406552.

45 Y.-Y. Zhang, F.-Y. Qiu, H.-T. Shi and W. Yu, *Chem. Commun.*, 2021, **57**, 3010–3013.

46 W. Yu, F.-Y. Qiu, S.-T. Luo, H.-T. Shi, G. Yuan and X. Wei, *Inorg. Chem. Front.*, 2021, **8**, 2356–2364.

47 R. Sekiya, M. Fukuda and R. Kuroda, *J. Am. Chem. Soc.*, 2012, **134**, 10987–10997.

48 M. Fukuda, R. Sekiya and R. Kuroda, *Angew. Chem., Int. Ed.*, 2008, **47**, 706–710.

49 Y. Yamauchi, M. Yoshizawa and M. Fujita, *J. Am. Chem. Soc.*, 2008, **130**, 5832–5833.

50 S. Freye, J. Hey, A. Torras-Galán, D. Stalke, R. Herbst-Irmer, M. John and G. H. Clever, *Angew. Chem., Int. Ed.*, 2012, **51**, 2191–2194.

51 S. Sato, O. Morohara, D. Fujita, Y. Yamaguchi, K. Kato and M. Fujita, *J. Am. Chem. Soc.*, 2010, **132**, 3670–3671.

52 S. Watanabe, M. Yamashina, E. Tsurumaki and S. Toyota, *ChemistryEurope*, 2023, **1**, e202300047.

53 D. Samanta and P. S. Mukherjee, *J. Am. Chem. Soc.*, 2014, **136**, 17006–17009.

54 P. Montes-Tolentino, A. S. Mikherdov, C. Drechsler, J. J. Holstein and G. H. Clever, *Angew. Chem., Int. Ed.*, 2025, **64**, e202423810.

55 T. Tateishi, Y. Yasutake, T. Kojima, S. Takahashi and S. Hiraoka, *Commun. Chem.*, 2019, **2**, 25.

56 Q.-Y. Hong, B. Huang, M.-X. Wu, J.-Y. Jiang, H.-B. Yang, X.-L. Zhao, G. H. Clever and X. Shi, *Nat. Commun.*, 2025, **16**, 2484.

57 Y.-W. Zhang, S. Bai, Y.-Y. Wang and Y.-F. Han, *J. Am. Chem. Soc.*, 2020, **142**, 13614–13621.

58 Y. Wang, Y. Zhang, Z. Zhou, R. T. Vanderlinden, B. Li, B. Song, X. Li, L. Cui, J. Li, X. Jia, J. Fang, C. Li and P. J. Stang, *Nat. Commun.*, 2020, **11**, 2727.

59 Y. Wang, T. Liu, Y.-Y. Zhang, B. Li, L. Tan, C. Li, X.-C. Shen and J. Li, *Nat. Commun.*, 2024, **15**, 1363.

60 J. Martí-Rujas, *Commun. Chem.*, 2025, **8**, 92.

61 T. Abe, Y. Zhang, K. Takeuchi and S. Hiraoka, *Chem*, 2025, **11**, 102453.

62 A. Carbonell, I. Izquierdo, D. B. Guzmán Ríos, G. Norjmaa, G. Ujaque, A. J. Martínez-Martínez and U. Pischel, *Inorg. Chem.*, 2024, **63**, 19872–19884.

63 D. L. Caulder, C. Brückner, R. E. Powers, S. König, T. N. Parac, J. A. Leary and K. N. Raymond, *J. Am. Chem. Soc.*, 2001, **123**, 8923–8938.

64 M. Scherer, D. L. Caulder, D. W. Johnson and K. N. Raymond, *Angew. Chem., Int. Ed.*, 1999, **38**, 1587–1592.

65 C. J. Hastings, M. D. Pluth, R. G. Bergman and K. N. Raymond, *J. Am. Chem. Soc.*, 2010, **132**, 6938–6940.

66 W. M. Hart-Cooper, C. Zhao, R. M. Triano, P. Yaghoubi, H. L. Ozores, K. N. Burford, F. D. Toste, R. G. Bergman and K. N. Raymond, *Chem. Sci.*, 2015, **6**, 1383–1393.

67 C. J. Brown, F. D. Toste, R. G. Bergman and K. N. Raymond, *Chem. Rev.*, 2015, **115**, 3012–3035.

68 S. M. Treacy, A. L. Smith, R. G. Bergman, K. N. Raymond and F. D. Toste, *J. Am. Chem. Soc.*, 2024, **146**, 29792–29800.

69 X.-S. Du, Y. Han and C.-F. Chen, *Chem. Commun.*, 2022, **58**, 1326–1329.

70 G. Wu, Y. Chen, S. Fang, L. Tong, L. Shen, C. Ge, Y. Pan, X. Shi and H. Li, *Angew. Chem., Int. Ed.*, 2021, **60**, 16594–16599.

71 M. Grajda, G. Staros, H. Jędrzejewska and A. Szumna, *Inorg. Chem.*, 2022, **61**, 11410–11418.

72 D. M. Dalton, S. R. Ellis, E. M. Nichols, R. A. Mathies, F. D. Toste, R. G. Bergman and K. N. Raymond, *J. Am. Chem. Soc.*, 2015, **137**, 10128–10131.

73 C. M. Hong, R. G. Bergman, K. N. Raymond and F. D. Toste, *Acc. Chem. Res.*, 2018, **51**, 2447–2455.

74 M. Morimoto, S. M. Bierschenk, K. T. Xia, R. G. Bergman, K. N. Raymond and F. D. Toste, *Nat. Catal.*, 2020, **3**, 969–984.

75 L. Liang and D. Astruc, *Coord. Chem. Rev.*, 2011, **255**, 2933–2945.

76 M. Meldal and C. W. Tornøe, *Chem. Rev.*, 2008, **108**, 2952–3015.

77 V. Martí-Centelles, T. K. Piskorz and F. Duarte, *J. Chem. Inf. Model.*, 2024, **64**, 5604–5616.

78 R. Zhu, J. Lübben, B. Dittrich and G. H. Clever, *Angew. Chem., Int. Ed.*, 2015, **54**, 2796–2800.

79 G. Li, T. K. Ronson, R. Lavendomme, Z. Huang, C. Fuertes-Espinosa, D. Zhang and J. R. Nitschke, *Chem*, 2023, **9**, 1549–1561.

80 W. Xue, E. Benchimol, A. Walther, N. Ouyang, J. J. Holstein, T. K. Ronson, J. Openy, Y. Zhou, K. Wu, R. Chowdhury, G. H. Clever and J. R. Nitschke, *J. Am. Chem. Soc.*, 2024, **146**, 32730–32737.

81 W. M. Bloch, S. Horiuchi, J. J. Holstein, C. Drechsler, A. Wuttke, W. Hiller, R. A. Mata and G. H. Clever, *Chem. Sci.*, 2023, **14**, 1524–1531.

82 P. Caravan and C. Orvig, *Inorg. Chem.*, 1997, **36**, 236–248.

83 (*a*) CCDC 2467878: Experimental Crystal Structure Determination, 2025, DOI: **10.5517/ccdc.csd.cc2nv0zj**; (*b*) CCDC 2467879: Experimental Crystal Structure Determination, 2025, DOI: **10.5517/ccdc.csd.cc2nv10l**.